Computers & Geosciences 87 (2016) 41–55

Contents lists available at ScienceDirect

Computers & Geosciences

journal homepage: www.elsevier.com/locate/cageo

Research Paper

Averaged ratio between complementary profiles for evaluating shape distortions of map projections and spherical hierarchical tessellations

Jin Yan, Xiao Song *, Guanghong Gong

School of Automation Science and Electrical Engineering, Beihang University, No. 37, Xueyuan Road, Haidian District, Beijing 100191, China

ARTICLE INFO

Article history:
Received 8 October 2014
Received in revised form
16 November 2015
Accepted 17 November 2015
Available online 19 November 2015

Keywords:
Spherical tessellation
Quantitative evaluation
Shape regularity
Distortion
Map projection

ABSTRACT

We describe a metric named averaged ratio between complementary profiles to represent the distortion of map projections, and the shape regularity of spherical cells derived from map projections or non-map-projection methods. The properties and statistical characteristics of our metric are investigated. Our metric (1) is a variable of numerical equivalence to both scale component and angular deformation component of Tissot indicatrix, and avoids the invalidation when using Tissot indicatrix and derived differential calculus for evaluating non-map-projection based tessellations where mathematical formulae do not exist (e.g., direct spherical subdivisions), (2) exhibits simplicity (neither differential nor integral calculus) and uniformity in the form of calculations, (3) requires low computational cost, while maintaining high correlation with the results of differential calculus, (4) is a quasi-invariant under rotations, and (5) reflects the distortions of map projections, distortion of spherical cells, and the associated distortions of texels. As an indicator of quantitative evaluation, we investigated typical spherical tessellation methods, some variants of tessellation methods, and map projections. The tessellation methods we evaluated are based on map projections or direct spherical subdivisions. The evaluation involves commonly used Platonic polyhedrons, Catalan polyhedrons, etc. Quantitative analyses based on our metric of shape regularity and an essential metric of area uniformity implied that (1) Uniform Spherical Grids and its variant show good qualities in both area uniformity and shape regularity, and (2) Crusta, Unicube map, and a variant of Unicube map exhibit fairly acceptable degrees of area uniformity and shape regularity.

1. Introduction

Spherical tessellation methods divide a sphere into spherical polygonal cells. Each cell can be further subdivided to produce hierarchical sub-cells in different level of details (Goodchild, 1994; Kimerling et al., 1999; Clarke, 2000; Sahr et al., 2003).

The tessellations of a sphere have been widely used in domains of cartography (Goodchild and Yang, 1992; Dutton, 1996; Górski et al., 2005; Holhoş and Roşca, 2014), virtual globe (Fekete and Treinish, 1990; Dutton, 1996; White, 2000; Sahr et al., 2003; Cignoni et al., 2003b; Platings and Day, 2004; Hwa et al., 2005; Westerteiger et al., 2011; Bernardin et al., 2011; Holhoş and Roşca, 2014), weather forecast (Majewski et al., 2002), geological analysis (Bernardin et al., 2011), environment mapping (Wan et al., 2007; Ho et al., 2011), atmospheric modeling (Ronchi et al., 1996), thermal convection calculation (Zhong et al., 2000; Choblet et al., 2007), microwave background analysis (Tegmark, 1996; Górski et al., 2005), etc.

Different kinds of tessellations exhibit their own characteristics and inherent advantages and disadvantages (Clarke, 2000). For the sake of comparison, we could place tessellations in different categories. Tessellations that belong to the same category exhibit similar characteristics. Tessellations in different categories may exhibit diversity in characteristics.

Spherical tessellations could be categorized as geographic coordinate system (GCS-)based grids, polyhedron-based grids, etc.

The common uses of GCS-based grids in virtual globes (e.g., Google Earth and NASA WorldWind) and the widely existing GCS-based datasets (e.g., Plate Carrée used in NASA WorldWind) provide simplicity and convenience. However, singularity and data redundancy are inevitable in these methods and datasets at two poles. Cells distort from equator to poles. Especially, quadrilateral cells would degenerate into triangle cells at the poles (Sahr et al., 2003; Bernardin et al., 2011; Oldham et al., 2012). In addition, area uniformity of cells is hard to achieve. Some map projections (e.g., Mercator projection and Lambert cylindrical equal-area

* Corresponding author.
E-mail addresses: kinian@126.com (J. Yan), songxiao@buaa.edu.cn (X. Song), ggh@buaa.edu.cn (G. Gong).

http://dx.doi.org/10.1016/j.cageo.2015.11.009
0098-3004/

projection) also suffer from severe distortions at the poles. Hence, Web Mercator is defined within the areas between ca. 85.05°S and 85.05°N.

Polyhedron-based methods avoid the singularity at two poles, produce similar areas and shapes of cells, and exhibit symmetry for each initial cell.

Sahr et al. (2003) have given an overview on discrete global grid system based on five Platonic polyhedrons. Platonic polyhedrons are commonly employed for polyhedron-based grids, e.g., cube (Ronchi et al., 1996; Hwa et al., 2005; Choblet et al., 2007; Ho et al., 2011; Roşca and Plonka, 2011), octahedron (Dutton, 1996; White, 2000; Holhoş and Roşca, 2014), icosahedron (Fekete and Treinish, 1990; Tegmark, 1996; White, 2000; Teanby, 2006).

Catalan polyhedrons are also used for polyhedron-based grids, e.g., rhombic dodecahedron (Zhong et al., 2000) and rhombic triacontahedron (Platings and Day, 2004; Bernardin et al., 2011).

Furthermore, Oldham et al. (2012) used two parameters to construct a generic polyhedron-based grid generation method. Special cases of their method involve some Platonic polyhedrons and some Catalan polyhedrons. Twelve faces (Górski et al., 2005), six faces (Wan et al., 2007), or two hemispheres (Rosca, 2010) based tessellations are also used in specific domains.

Although polyhedron-based methods have the advantages of (1) non-singularity at two poles, (2) similar areas, and (3) similar shapes over GCS-based grids, recursive subdivisions or specific transformations between local coordinate system and GCS are usually required for raster or vector datasets.

Spherical tessellations could also be categorized as map projection (MP-)based methods, direct spherical subdivision (DSS-) based methods, etc.

MP-based tessellation methods (e.g., Dutton, 1996; Ronchi et al., 1996; Górski et al., 2005; Wan et al., 2007; Rosca, 2010; Ho et al., 2011; Roşca and Plonka, 2011; Holhoş and Roşca, 2014) subdivide regular grids on a plane initially. Then, spherical grids are constructed by some inverse projection formulae. The boundaries of MP-based grids are geodesics, graticules, or some forms of complicated curves.

Instead, DSS-based tessellation methods (e.g., Fekete and Treinish, 1990; Zhong et al., 2000; Majewski et al., 2002; Bernardin et al., 2011) directly subdivide cells on a sphere via great circle arcs. In general, DSS-based methods are constructed recursively. The vertex coordinates and boundary coordinates of a sub-cell are calculated according to the coordinates of its parents. Usually, DSS-based methods are unable to produce equal-area tessellations.

Above categorizations provide qualitative means to identify characteristics of spherical tessellations. In addition, Goodchild Criteria (Goodchild, 1994) and its revised criteria (Kimerling et al., 1999) formulated more qualitative criteria to evaluate spherical tessellation methods. In addition, Clarke (2000) has given an overview on global georeferencing system, and discusses different aspects of criteria and metrics.

Moreover, it should also take consideration of some quantitative metrics, such as area (Snyder, 1987; Dutton, 1996; Kimerling et al., 1999; Oldham et al., 2012), distortions (Snyder, 1987; Mulcahy and Clarke, 2001), compactness (Kimerling et al., 1999; Gregory et al., 2008), grid point spacing (Kimerling et al., 1999), and mesh quality for numerical calculation (Gregory et al., 2008; Oldham et al., 2012).

Area metrics have been extensively studied and commonly used (e.g., Dutton, 1996; Kimerling et al., 1999; Oldham et al., 2012), while distortion of shape may still need to be investigated.

Different topologies of shape (e.g., triangular, quadrilateral, or hexagonal grids) are used in different applications. Among these shapes, quadrilateral subdivisions are suitable for array storage (Kimerling et al., 1999) and provide convenient ways to map textures or construct quadtrees. Mapping from sphere to quadrilateral grids can be employed in the domains of cartography, virtual globes, environment mapping, etc.

When we map a sphere by quadrilateral grids, quadtrees-based pyramid is an essential means to provide high-resolution details of texture mapping (Platings and Day, 2004; Bernardin et al., 2011). In these applications, the globe is tessellated into quadrilateral cells. Within cells, adaptive unstructured triangulation (Bahrainian and Dezfuli, 2014), regular triangulation (Bösch et al., 2009), or irregular triangulation (Cignoni et al., 2003a) may be constructed. Then, the underlying texture is mapped for each cell.

Triangular cells are compatible with quadrilateral cells (White, 2000). For example, in some methods (Cignoni et al., 2003a,b; Hwa et al., 2005; Gobbetti et al., 2006; Bösch et al., 2009; Goswami et al., 2010), triangular nodes are employed for representing meshes, and adjacent triangular nodes are connected together as quadrilateral cells for data storage and texture mapping.

No matter what kinds of map projections or DSS are used, texels (i.e., pixels on textures) are evenly sampled, but they become uneven when mapping onto a sphere (Wan et al., 2007; Ho et al., 2011). Distortions of cells and texels inevitably occur in the applications mentioned above. The most distorted cell may result in severe distortion of texels. Thus, it is a practical issue to measure the distortions and compare the degree of distortions for different tessellation methods.

It should be noted that viewing parameters and perspective projection could also result in distortion of texels. These view-dependent distortions are beyond the scope of our paper.

Much research (Snyder, 1987; Mulcahy, 2000; Mulcahy and Clarke, 2001; White, 2006; Bauer-Marschallinger et al., 2014) on the distortion of/between map projections has been carried out. These methods provide various means to measure distortions of MP-based tessellations, while distortions of non-MP-based tessellations (e.g., DSS-based tessellations) still need to be investigated.

Oldham et al. (2012) used diagonal ratio of great circle arcs (DiRaGCa) to evaluate their generic polyhedron-based grid generation method. The metric DiRaGCa is also suitable for MP-based tessellations, but DiRaGCa is inaccurate in some cases (e.g., degenerated quadrilateral, and rectangle-like quadrilateral).

Mulcahy and Clarke (2001) have given an overview on symbolization of map projection distortion. Tissot indicatrix provides a visual representation to illustrate map projection distortions (Mulcahy and Clarke, 2001). Tissot extensively analyzed the distortion of map projections by using an infinitely small circle on a sphere and projecting it onto a plane by specific map projection. Generally, the circle on a sphere turns to be an ellipse with a semi-major axis and a semi-minor axis. Tissot ellipses intuitively reflect map distortions. In addition, some differential calculus (Snyder, 1987, pp. 21–24) could also reflect areal, linear, or angular distortions of map projections.

Although Tissost ellipses are intuitive and elegant, a disadvantage of Tissot indicatrix is that (1) the indicatrix only represents distortions of infinitesimal areas near the center of ellipses and (2) the indicatrix is limited to the forward transformation from the globe to a map projection (Mulcahy and Clarke, 2001). There is neither projection plane(s) nor transformation formulae for DSS-based tessellation methods, hence, Tissot indicatrix is also limited to MP-based tessellation methods only. Those complicated numerical methods described in Snyder (1987) and Mulcahy (2000) also suffer from these limitations.

To avoid the disadvantages mentioned above, we introduce the averaged ratio between complementary profiles (AveRaComp) to measure the shape regularity of spherical cells. The metric AveRaComp consists two complementary metrics, diagonal ratio of small circle arcs (DiRaSCa), and a ratio representing the divergence of angle between diagonals (RaReDad). Experimental comparisons

and analyses imply that the metric AveRaComp is highly correlated with the numerical methods described in Snyder (1987) and Mulcahy (2000), and avoid invalidation for non-MP-based tessellations.

For one cell, the metric AveRaComp is fairly acceptable and effective to reflect the distortions of the cell and associated distortions of texture mapping. The maximum value of AveRaComp (MaxAveRaComp) could be calculated to represent the shape regularity or texel distortion for all cells in a given level of tessellation. Then, the suprema of MaxAveRaComp are calculated to evaluate and compare different tessellation methods.

2. Metrics of shape regularity

2.1. Preliminaries

Taking Uniform Spherical Grids (USG) (Roşca and Plonka, 2011) for example, the construction of MP-based tessellations are usually as follows: (1) tiling regular grids on projection planes [see Fig. 1 (a)] and (2) transforming straight lines of planar grids to produce the boundaries of spherical cells via specific inverse transformation [see Fig. 1(b)].

Tessellating each planar square into four equal-area squares makes it possible to construct hierarchical subdivisions. The midpoints of the square' edges and the barycentric point [i.e., the geometric center of planar square, marked as red stars in Fig. 1(a)] in each square are used to subdivide the corresponding cell into four sub-cells and produce hierarchical tilings on a sphere. The corresponding "center points" on a sphere are just the common points of four subdivided sub-tiles.

Similarly, Fig. 1(c) illustrates the process of construction quadrilateral grids by using zenithal orthotriangular (ZOT) projection (Dutton, 1991). Originally, Dutton (1996) used ZOT projection to construct his octahedral quaternary triangular mesh (O-QTM). Hence, we refer the quadrilateral version of grids in Fig. 1 (c) as O-QTM/Quad.

In addition, a variant of USG is to be investigated. As illustrated in Fig. 2(a), this variant is constructed by initially subdividing planar grids of USG via diagonals, then combining adjacent triangles. Similarly, we could convert other cube (or six-faces) based tessellations into rhombic dodecahedron (or twelve-faces) based tessellations, or vice versa. Conversions between octahedron-based tessellations and two-hemispheres based tessellations are possible [see Fig. 2(c)]. These kinds of variants are named with a postfix "/Diag". The initial polyhedron of USG/Diag is a rhombic dodecahedron. The initial cells of O-QTM/Quad/Diag are two hemispheres.

Additionally, another two triangular tessellations will be investigated in this paper, i.e., octahedral equal area partition (OEAP) (Holhoş and Roşca, 2014) and icosahedron-based sphere quadtrees (SQT) (Fekete and Treinish, 1990). For simplicity, we refer the quadrilateral versions of OEAP and SQT as OEAP/Quad and SQT/Quad, respectively. Cubed Sphere (Ronchi et al., 1996) and New Uniform Grids (Rosca, 2010) are also abbreviated to C-Sph and NUG in this paper.

Opposite to MP-based tessellations, projection plane(s) may not exist in some other tessellation methods (e.g., DSS-based tessellations). Thus, center points of cells may not exist either. But when a cell is subdivided, the common point of four sub-cells still exists. The common point plays an important role in tessellations. In Section 2.2, we will describe our metric AveRaComp by using the common point of four sub-cells. In Section 2.3, we will give an analysis based on numerical calculations to validate our metric. In Section 2.4, we will discuss and explain some known issues of our metric. In Section 2.5, we will simplify our AveRaComp metric for the reason of compatible with reference ellipsoid.

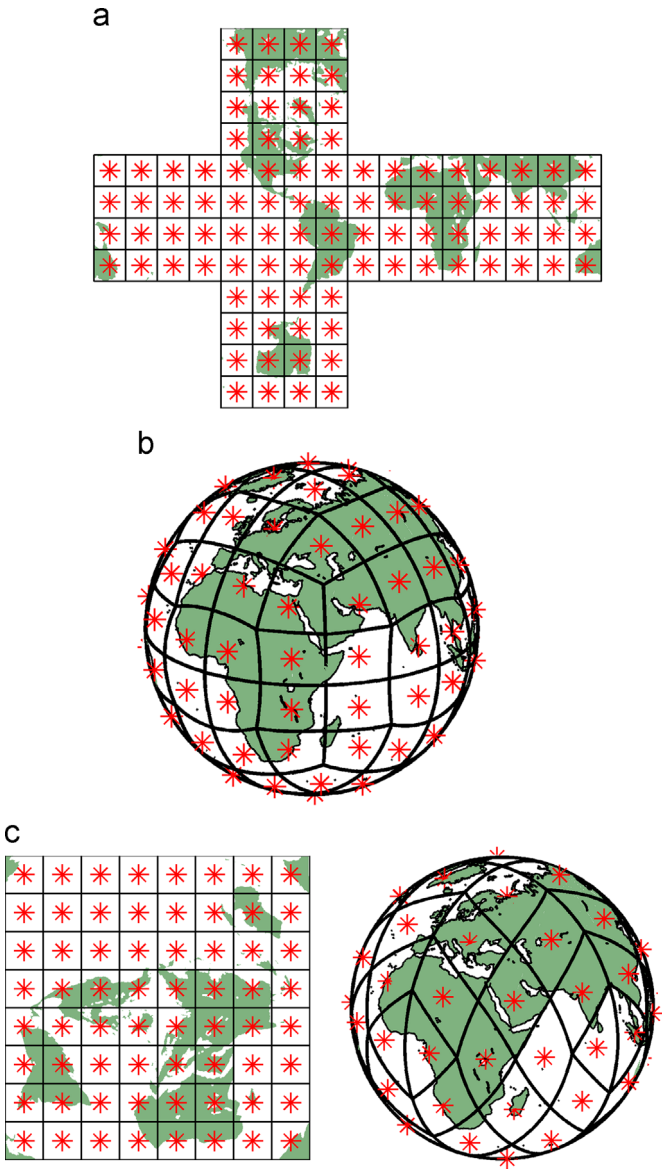

Fig. 1. Two MP-based spherical tessellation methods. Red stars represent center points of grids on projection plane(s). They are also the common points of further subdivided sub-cells. (a) Regular grids on six projection planes using USG method (Roşca and Plonka, 2011). (b) Spherical quadrilateral cells of USG method. (c) Planar grids and spherical cells of O-QTM/Quad by using ZOT projection (Dutton, 1991). Some quadrilateral cells of O-QTM/Quad degenerate into triangle cells. (For interpretation of the references to color in this figure caption, the reader is referred to the web version of this paper.)

2.2. Averaged ratio between complementary profiles

Fig. 3 illustrates a spherical quadrilateral cell (denoted by $\diamond P_1P_2P_3P_4$) on the Earth. The point P_* is the common point of sub-cells of $\diamond P_1P_2P_3P_4$. The small circle arc connecting points P_s, P_*, and P_t is denoted by $\overset{\frown}{P_sP_*P_t}$.

We employ $\rho_{CP}(i)$, the averaged ratio between complementary profiles (AveRaComp) to evaluate the shape regularity of $\diamond P_1P_2P_3P_4$. The metric $\rho_{CP}(i)$ consists of two profiles. One is $\rho_{D3}(i)$, the diagonal ratio of small circle arcs (DiRaSCa), and another is $\rho_{\alpha}(i)$, a ratio

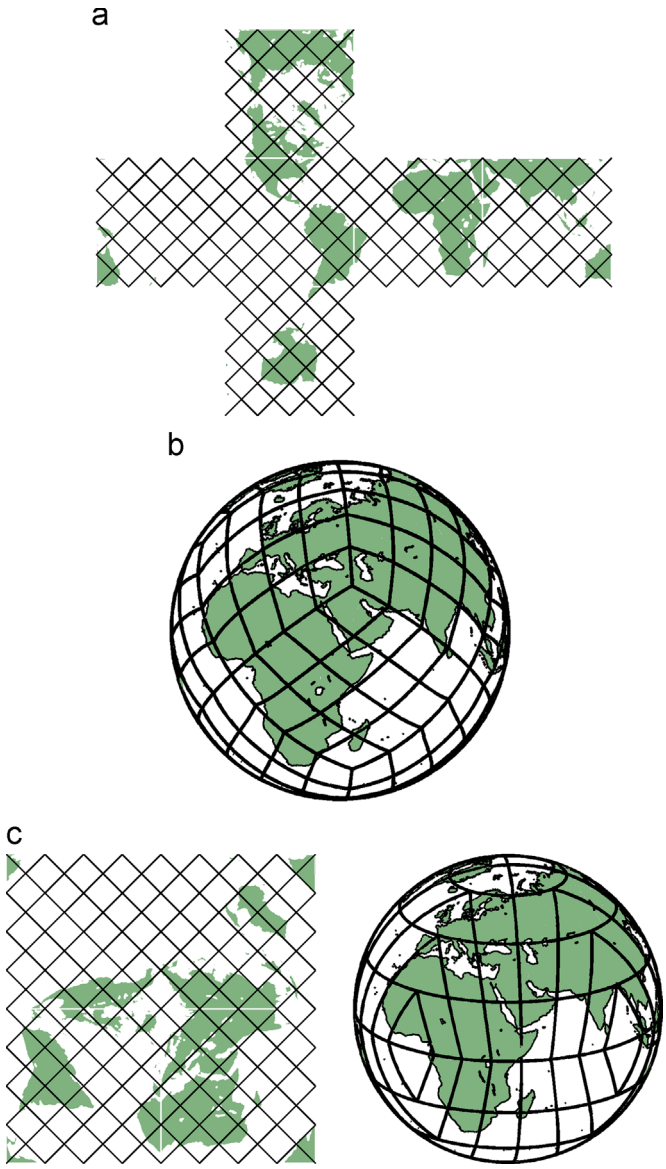

Fig. 2. Variants of USG method and O-QTM/Quad method. (a) Planar tessellations of USG/Diag. (b) Spherical tessellations of rhombic dodecahedron based USG/Diag. (c) Planar grids and spherical cells of O-QTM/Quad/Diag based on two hemispheres. Some quadrilateral cells of O-QTM/Quad/Diag degenerate into triangle cells.

representing the divergence of angle between diagonals (RaReDad). Both $\rho_{D3}(i)$ and $\rho_{\alpha}(i)$ are dimensionless quantities, so we could synthesize these two metrics as a whole.

$$\rho_{CP}(i) = [\rho_{D3}(i) + \rho_{\alpha}(i)]/2, \tag{1}$$

$$\rho_{D3}(i) = \frac{\max(|\widehat{P_1P_*P_3}|, |\widehat{P_2P_*P_4}|)}{\min(|\widehat{P_1P_*P_3}|, |\widehat{P_2P_*P_4}|)}, \tag{2}$$

$$\rho_{\alpha}(i) = \cot\left(\frac{1}{2}\arccos|\overrightarrow{P_1P_*P_3}\cdot\overrightarrow{P_2P_*P_4}|\right), \tag{3}$$

where i is the index of the cell $\diamond P_1P_2P_3P_4$, $|\widehat{P_sP_*P_t}|$ is the length of small circle arc $\widehat{P_sP_*P_t}$, and $\overrightarrow{P_sP_*P_t}$ is the normalized vector that is tanget to $\widehat{P_sP_*P_t}$ at point P_*.

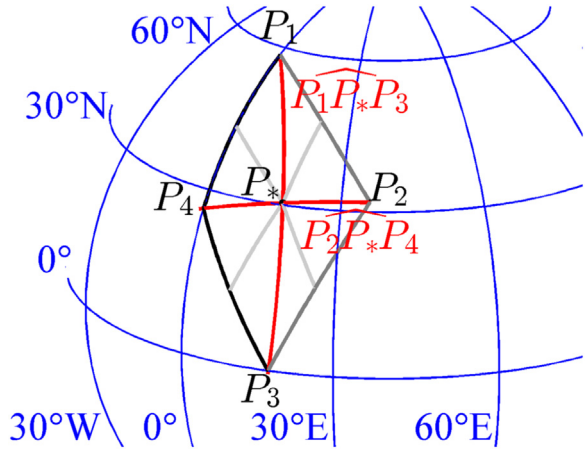

Fig. 3. The spherical quadrilateral $\diamond P_1P_2P_3P_4$ represents the ith spherical cell of a given tessellation method, where $i = 1, 2, \ldots, N$, and N is the total number of cells. The point P_* is the common point of four sub-cells of $\diamond P_1P_2P_3P_4$. The arcs in red represent small circle arcs $\widehat{P_1P_*P_3}$ and $\widehat{P_2P_*P_4}$. (For interpretation of the references to color in this figure caption, the reader is referred to the web version of this paper.)

Vector $\overrightarrow{P_sP_*P_t}$ and the length of $\widehat{P_sP_*P_t}$ in Eqs. (2) and (3) is calculated according to

$$\overrightarrow{P_sP_*P_t} = \frac{\vec{t}}{|\vec{t}|} \tag{4}$$

$$|\widehat{P_sP_*P_t}| = |\vec{p}_*||\vec{c} - \vec{p}_*|\cdot\arccos\left[\frac{(\vec{c} - \vec{p}_s)\cdot(\vec{c} - \vec{p}_t)}{|\vec{c} - \vec{p}_s|\cdot|\vec{c} - \vec{p}_t|}\right], \tag{5}$$

where $\vec{t} = (\vec{c} - \vec{p}_*/|\vec{p}_*|)/|\vec{c} - \vec{p}_*/|\vec{p}_*|| \times \vec{n}$, $\vec{c} = k\cdot\vec{n}$, $k = \vec{n}\cdot\vec{p}_*/|\vec{p}_*|$, $\vec{n} = (\vec{p}_* - \vec{p}_s) \times (\vec{p}_* - \vec{p}_t)/|(\vec{p}_* - \vec{p}_s) \times (\vec{p}_* - \vec{p}_t)|$, and the vectors $\vec{p}_s$, $\vec{p}_*$, and $\vec{p}_t$ are the Cartesian coordinates of the points P_s, P_*, and P_t.

According to the definitions in Eqs. (2) and (3), $\rho_{D3}(i) \geq 1$, and $\rho_{\alpha}(i) \geq 1$. Thus, our shape metric AveRaComp $\rho_{CP}(i) \geq 1$.

Then, we can calculate ρ_{CP}, the maximum value of AveRaComp (MaxAveRaComp) for all cells to evaluate the shape regularity of spherical tessellations.

$$\rho_{CP} = \max_{i=1}^{N} \rho_{CP}(i), \tag{6}$$

where N is the total number of cells.

The geometry meanings of the metrics $\rho_{D3}(i)$ and $\rho_{\alpha}(i)$ of a planar quadrilateral are demonstrated in Fig. 4. Diamonds and rectangles are two special cases of a planar quadrilateral. For a diamond, the metric $\rho_{D3}(i) = |AD|/|BC|$ measures one profile of distortion, i.e., the length ratio between the maximum diagonal and the minimum diagonal. For a rectangle, the metric $\rho_{\alpha}(i) = |EG|/|EF|$ measures another profile of distortion, the length ratio between the maximum edge and the minimum edge. By synthesizing above complementary metrics, the average of metrics $\rho_{D3}(i)$ and $\rho_{\alpha}(i)$ could measure the shape distortions of arbitrary quadrilaterals in addition to diamonds or rectangles. In Section 2.3, we will evaluate the accuracy of our metric $\rho_{CP}(i)$ by measuring the shape distortions of spherical quadrilaterals.

Quadrilateral subdivisions are commonly used in virtual globes, environment mapping, etc. Among these methods, quadrilateral cells are usually used for texture mapping, so the metrics AveRaComp or MaxAveRaComp may reflect the distortion of texels. In Section 3.2, we will give an experimental analysis on our metrics.

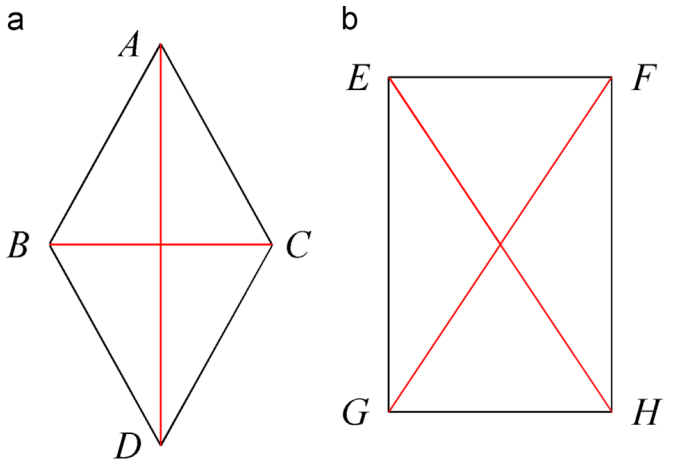

Fig. 4. Illustration of two special cases of a planar quadrilateral. For a diamond, $\rho_{D3}(i) = |AD|/|BC| > 1$, and $\rho_\alpha(i) = 1$. For a rectangle, $\rho_{D3}(i) = 1$, and $\rho_\alpha(i) = |EG|/|EF| > 1$. Therefore, the diagonal ratio $\rho_{D3}(i)$ dominates in a diamond, while the edge ratio $\rho_\alpha(i)$ dominates in a rectangle. The average between $\rho_{D3}(i)$ and $\rho_\alpha(i)$ could reflect both aspects for arbitrary quadrilaterals.

White (2000) mentioned that triangular cells are compatible with quadrilateral cells, so we can evaluate the shape regularity of the quadrilateral cells derived from the triangular cells. Generally, a texel is square even though triangular cells (Cignoni et al., 2003a, b; Hwa et al., 2005; Gobbetti et al., 2006; Bösch et al., 2009; Goswami et al., 2010) are used for texture mapping, so the metrics AveRaComp or MaxAveRaComp could also reflect the distortion of texels of triangular cells.

In addition to quadrilateral and triangular cells, spherical hexagonal cells also provide a possible means to subdivide a sphere. It should be noted that one disadvantage of our metric is the unsuitability for evaluating hexagonal cells. But it is unnecessary to compare the shape regularity of hexagonal cells with the shape regularity of quadrilateral cells due to the differences of topology between hexagonal and quadrilateral cells.

It should also be noted that it is impossible to completely tile a sphere by hexagons individually. Pentagons are inevitable at the vertices of initial polyhedrons. Besides, tessellations using hexagons do not satisfy a hierarchical structure (White, 2000; Sahr et al., 2003).

Due to the disadvantages of hexagonal cells mentioned above and the differences of topology between hexagonal and quadrilateral cells, we do not consider hexagonal cells in this paper.

2.3. Other metrics of shape regularity

Oldham et al. (2012) used the diagonal ratio of great circle arcs (DiRaGCa) to evaluate his generic grid generation method. The metric DiRaGCa reflects the shape regularity of cells to some extent, especially for cells with diamond-like shape. But the metric DiRaGCa is inaccurate for cells with rectangle-like shape (see Fig. 4) or degenerated quadrilateral [see triangular cells in Figs. 1 (c) and 2(c)].

Tissot indicatrix is an intuitive assessment method for map projection distortions. Spherical cells of nine MP-based tessellations are investigated. Due to symmetry, we only investigate one or two initial cell(s) (see Fig. 5) for each method. The first and fourth rows of Fig. 6 depict Tissot ellipses for all MP-based spherical cells illustrated in Fig. 5. From the illustration, we obtain that ellipses in equatorial regions are more oblate than other regions when we use ZOT projection, projection of OEAP, or projection of NUG. Some Tissot ellipses of NUG are of heart-like shape, this misinterpretation is caused by the inherent weakness of Tissot

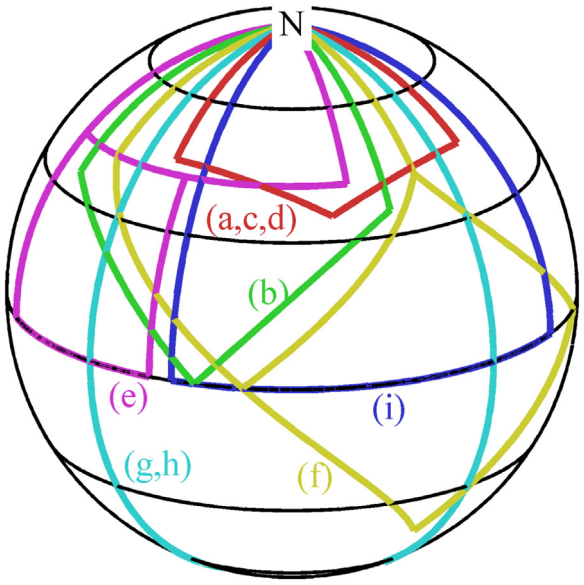

Fig. 5. Spherical regions on a sphere for evaluating different tessellations by using different shape indicators in Fig. 6. For clarity, we separate some regions by offsets along longitudinal direction. The letters in parentheses are corresponding to letters in Fig. 6.

indicatrix (Mulcahy and Clarke, 2001). In addition, projection of Unicube, USG, USG/Diag, and C-Sph exhibit less distortion than other methods.

To quantitatively evaluate the distortions of MP-based methods illustrated in the first and fourth rows of Fig. 6, we calculate the ratio $\rho_s = |a/b|$, where a and b are the maximum and minimum scale factor, respectively, by using (Eqs. (7)–13) mentioned by Snyder (1987). For all methods we investigated, we further calculate ω (see Eq. (14)), an indicator of angular deformation, to evaluate our AveRaComp metric. The correlation coefficients between ω and AveRaComp are also listed in Table 1.

$$h = \frac{1}{R}\sqrt{\left(\frac{\partial x}{\partial \phi}\right)^2 + \left(\frac{\partial y}{\partial \phi}\right)^2}, \tag{7}$$

$$k = \frac{1}{R\cos\phi}\sqrt{\left(\frac{\partial x}{\partial \lambda}\right)^2 + \left(\frac{\partial y}{\partial \lambda}\right)^2}, \tag{8}$$

$$\sin\theta' = \frac{1}{hkR^2\cos\phi}\left(\frac{\partial y}{\partial \phi}\frac{\partial x}{\partial \lambda} - \frac{\partial x}{\partial \phi}\frac{\partial y}{\partial \lambda}\right), \tag{9}$$

$$a' = \sqrt{h^2 + k^2 + 2hk\sin\theta'}, \tag{10}$$

$$b' = \sqrt{h^2 + k^2 - 2hk\sin\theta'}, \tag{11}$$

$$a = \frac{a' + b'}{2}, \tag{12}$$

$$b = \frac{a' - b'}{2}, \tag{13}$$

$$\omega = 2\arcsin(b'/a'), \tag{14}$$

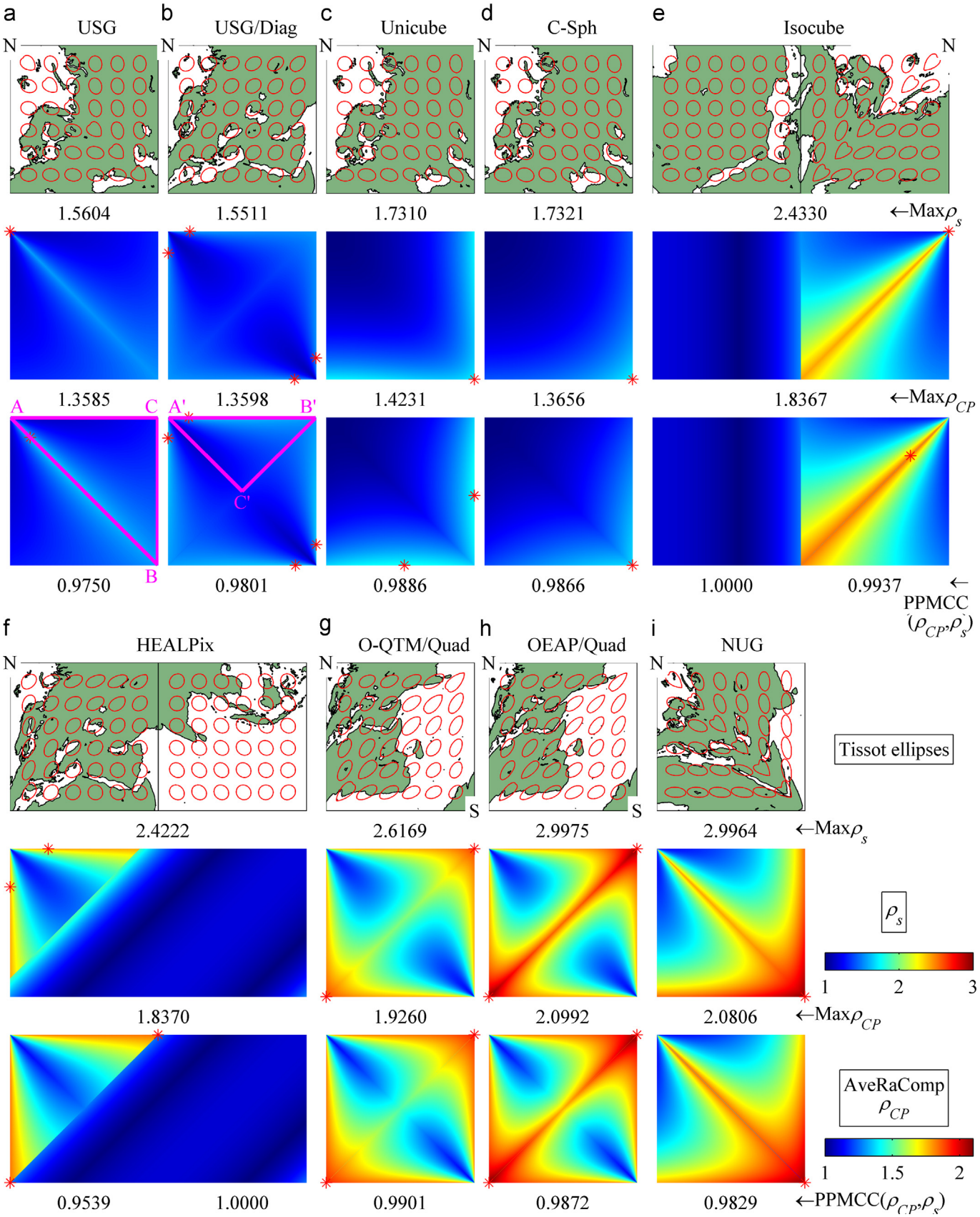

Fig. 6. Illustrations and comparisons of different shape indicators [Tissot ellipses, the ratios between the maximum and minimum scale factor (denoted by ρ_s), and our AveRaComp metric (denoted by ρ_{CP})]. Nine MP-based tessellations are investigated. The values above distributions are the maximum value for given tessellations. The positions of the maximum values are approximately coincident or adjacent (see red stars). Pearson product-moment correlation coefficients (PPMCCs) between ρ_s and ρ_{CP} for all tessellations we investigated are larger than 0.95, that means our metric ρ_{CP} has a high correlation with the metric ρ_s. It should be noted that PPMCCs are independent on the time of samples when the time of samples is large enough. Here, PPMCC is calculated using 1024×1024 samples (which is sufficient) for each tessellation. (For interpretation of the references to color in this figure caption, the reader is referred to the web version of this paper.)

Table 1
Pearson product-moment correlation coefficient (PPMCC) between different metrics (i.e., ρ_{D3}, ρ_α, and $\rho_{CP} = \rho_{D3} + \rho_\alpha$) and ρ_s (as a reference variable). There is a strong correlation between our metric ρ_{CP} and the reference metric ρ_s. Because both ρ_{CP} and ρ_s are ratios between two variables, it is intuitive to compare ρ_{CP} with ρ_s. We also notice that there is a strong correlation between ρ_s and a dimensionless quantity Tissot' omega ω. The numerical results also indicate that our metric ρ_{CP} could represent the distributions of Tissot' omega. In Section 2.5, we derive $\tilde{\rho}_{CP}$, a simplified version of AveRaComp to adapt for reference ellipsoid. The minimum value of PPMCC(ρ_{CP}, $\tilde{\rho}_{CP}$) for all methods we investigated is larger than 0.99998, hence, $\tilde{\rho}_{CP}$ is an estimate of ρ_{CP} in concise and general form (see Section 2.5).

Method		PPMCC (ρ_{D3}, ρ_s)	PPMCC (ρ_α, ρ_s)	PPMCC (ρ_{CP}, ρ_s)	PPMCC (ρ_{CP}, ω)	PPMCC (ω, ρ_s)	PPMCC (ρ_{CP}, $\tilde{\rho}_{CP}$)
NUG		0.2517	0.9314	0.9829	0.9817	0.9932	>0.9999
USG		0.6469	0.9395	0.9750	0.9745	0.9990	>0.9999
Unicube		0.6052	0.8041	0.9886	0.9885	0.9973	>0.9999
C-Sph		0.8454	0.5211	0.9866	0.9880	0.9976	>0.9999
Isocube	(polar)	0.9467	0.9516	0.9960	0.9974	0.9960	>0.9999
	(equatorial)	−0.1623	1.0000	1.0000	0.9979	0.9978	>0.9999
OEAP/Quad		0.8822	0.3823	0.9872	0.9851	0.9932	>0.9999
O-QTM/Quad		0.7922	0.7363	0.9901	0.9864	0.9950	>0.9999
HEALPix	(polar)	0.8969	0.9054	0.9539	0.9513	0.9912	>0.9999
	(equatorial)	1.0000	0.0819	1.0000	0.9985	0.9985	>0.9999
USG/Diag		0.9427	0.6651	0.9801	0.9791	0.9990	>0.9999

where R is the radius of the Earth, x and y are rectangular coordinates on projection plane(s), ϕ and λ are latitude and longitude. We notice that (Eqs. (7)–14) are derived from an assumption of the Earth being a sphere. Analyses of ρ_s and ω on Ellipsoid could also be conducted by using correction factors (Snyder, 1987, pp. 24–27).

We calculate metrics ρ_s and ω by the finite difference method. The distributions of ρ_s and the maximum value of ρ_s are illustrated in the second and fifth rows of Fig. 6. The ratio quantitatively represents the degrees of oblateness for ellipses. In addition, the metric ρ_s is a continuous function, any (x, y) belongs to it domain is valid. Further calculations imply that ω is also a continuous function, and has a similar distribution to ρ_s [see PPMCC(ω, ρ_s) in Table 1].

We also calculate our metrics AveRaComp and MaxAveRaComp for the same spherical tessellations. The distributions of our metric are illustrated in the third and sixth rows of Fig. 6. Our metric AveRaComp is a discrete function, the domain of AveRaComp is the set of projected points corresponding to the centers of all cells.

Red stars in Fig. 6 indicate the points of maximum values. The number above each distribution (ρ_s or ρ_{CP}) in Fig. 6 is the maximum value for corresponding tessellation. Pearson product-moment correlation coefficient (PPMCC) between ρ_s and ρ_{CP} is also represented in Fig. 6. PPMCC is the ratio between the covariance of two variables and the product of their standard deviations.

According to Eq. (1), our AveRaComp metric reflects two profiles of shape distortions of cells, while ρ_s reflects the ratio between the maximum and minimum directions. Although a little difference between ρ_{CP} and ρ_s exists in Fig. 6, we find that the distributions of these two metrics are fairly similar. The positions of MaxAveRaComp coincide with or adjoin the positions of maximum values of ρ_s.

Table 1 gives quantitative analyses of Fig. 6 by using PPMCCs within the range of −1 to 1, where −1 means total negative correlation, and 1 means total positive correlation. From Table 1, we obtain that PPMCCs between ρ_{CP} and ρ_s for all tessellations we investigated are larger than 0.95, so, there is a high correlation relationship between ρ_{CP} and ρ_s. While neither ρ_{D3} nor ρ_α could estimate the distortion of tessellations properly. From Table 1, PPMCCs(ρ_{CP}, ω) are also larger than 0.95, hence our AveRaComp simultaneously gives a good estimation of angular deformation of spherical tessellations. Furthermore, Fig. 7 indicates that ranking above nine tessellations in Fig. 6 according to MaxAveRaComp and the maximum values of ρ_s are also consistent (PPMCC=0.995).

In addition to polyhedron-based map projections, We evaluate

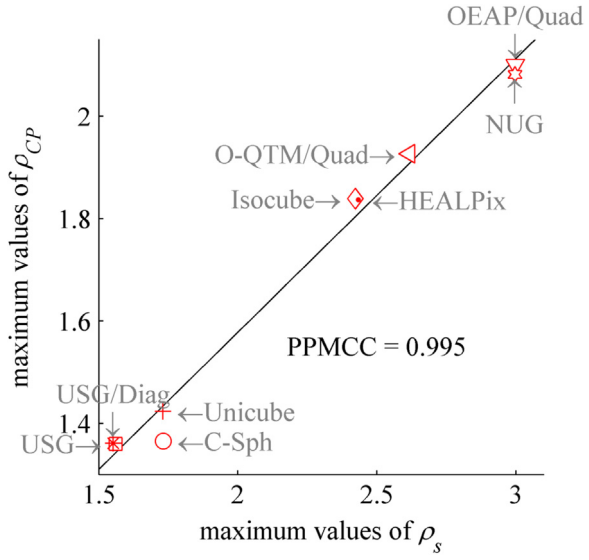

Fig. 7. Correlation between the maximum values of ρ_s and our metric MaxAveRaComp.

Plate Carrée projection and Web Mercator projection by using different metrics. For Plate Carrée projection, PPMCC(ρ_{CP}, ρ_s) = 1.0000, and PPMCC(ρ_{CP}, ω) = 0.9199. That means a strong correlation exists between our AveRaComp and ρ_s (or ω). For Web Mercator projection, metrics ρ_{CP}, ρ_s, and ω are approximately constant functions ($\rho_{CP} \approx 1.0000$, $\rho_s \approx 1.0000$, and $\omega \approx 0.0000$, the standard deviation of these metrics is less than 10^{-6}) where latitude $\phi \in [85°S, 85°N]$.

From above analyses, one benefit from our metric is that Eqs. (1)–(5) exhibit lower time complexity than differential calculus using (Eqs. (7)–14), while our metric ρ_{CP} produces similar shape distributions as those complicated formulae, and gives good estimates of the shape distortions indicator ρ_s, and the maximum angular deformation indicator ω. Another benefit from our metric AveRaComp is that it may be possible to evaluate non-MP-based tessellation methods. In Section 3.2, we will evaluate some DSS-based methods via our metric.

Table 2 lists the PPMCCs of AveRaComp between some original tessellations and their variants via transformations as illustrated in Fig. 2. Taking the comparison between USG and USG/Diag for

Table 2
PPMCCs of AveRaComp between some tessellations and their variants under rotations.

Method 1	Method 2	PPMCC (ρ_{CP1}, ρ_{CP2})
USG	USG/Diag	0.9977
Unicube	Unicube/Diag	0.9988
C-Sph	C-Sph/Diag	0.9981
O-QTM/Quad	O-QTM/Quad/Diag	0.9989
OEAP/Quad	OEAP/Quad/Diag	0.9991
Isocube (equ.)	Isocube/Diag (equ.)	0.9953
Isocube (equ.)	Isocube/Diag (pol.)	0.9985
Isocube (pol.)	Isocube/Diag (pol.)	0.9992
HEALPix (pol.)	HEALPix/Diag (pol.)	0.9992
HEALPix (pol.)	HEALPix/Diag (equ.)	0.9985
HEALPix (equ.)	HEALPix/Diag (equ.)	0.9953

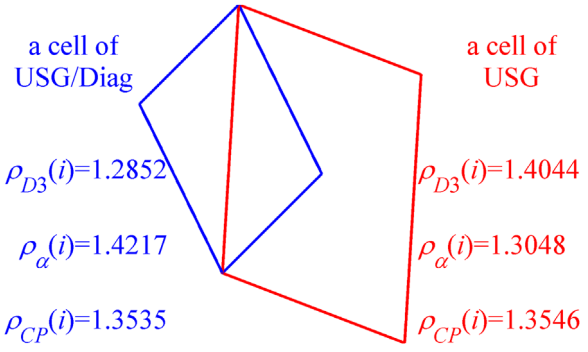

Fig. 8. Characteristics of quasi-invariant under rotations. Our metric $\rho_{CP}(i)$ for a cell of USG/Diag is approximately equal to the metric $\rho_{CP}(i)$ for an adjacent cell of USG.

example, half region of USG [see right triangle ABC in Fig. 6(a)] and quarter region of USG/Diag [see right triangle $A'B'C'$ in Fig. 6(b)] are numerically compared by using PPMCC. We notice that the length of AB is $1024\sqrt{2}$, while the length of $A'B'$ is 1024, so we resize both $\triangle ABC$ and $\triangle A'B'C'$ (by interpolation) to a pair of congruent triangles whose lengths of hypotenuses are $512\sqrt{2}$ for calculating PPMCCs. The results listed in Table 2 are larger than 0.99, so there is a strong correlation relationship between original tessellations and their variants. A cell of USG method and an adjacent cell of USG/Diag are illustrated in Fig. 8. Our metrics AveRacomp for these two cells are similar. Differences of AveRacomp mainly occur on boundaries or diagonals in above methods, hence PPMCCs between these methods are not totally equal to 1. Nevertheless, numerical results reveal that our metric AveRacomp is a quasi-invariant under rotations as illustrated in Fig. 2. Given a tessellation method T and its variant T', quasi-invariant under rotations means that $\rho_{CP}(C) \approx \rho_{CP}(C')$, where C is a cell of T, C' is a cell of T', and C and C' locate in an approximately same position on Earth. Because cells are located in discrete positions, C and C' may not coincide strictly. We do not calculate PPMCCs of ρ_s between methods listed in Table 2, because ρ_s is not the key point of our paper. But a fact is that ρ_s is also a quasi-invariant under rotations.

2.4. Further discussions

In summary, our metric (1) could quantitatively measure the shape regularity of spherical cells by using uniform formula for both MP-based and non-MP-based tessellations, and (2) exhibits good estimation, similar distributions, and consistent rankings as differential calculus when we evaluate MP-based tessellations (see Section 2.3).

In our method, we only employ vertices of cells to measure the shape regularity of tessellations. It seems that our metric does not depend on the shape of boundaries explicitly. Alternatively, we only use four corners and one midpoints in Eq. (1). Therefore, there are still two issues need to be discussed, one is the choice of points in our metric, and another is the influences of boundary of cells on our metric.

Firstly, the choices of points in our metric are not arbitrary. For a cell and its four sub-cells on a sphere, we select the common point of four sub-cells as the midpoint in our metric. Strictly speaking, for MP-based tessellation methods, the midpoint of a cell is just the barycentric point of the cell.

Although our metric involves coordinates of only five points, utilizing small circle arcs via these five points are important to measure shape regularity, and representative of both interior and margins of cells. In other words, using small circle arcs via midpoint of a cell could avoid any deviation of diagonal to one boundary. Deviation of diagonal to one boundary may occur in the case of degenerated quadrilateral [see triangular cells in Figs. 1 (c) and 2(c)] when using great circle arcs.

Secondly, the boundaries of a cell seem to have no influence on our metric if we fix the five points in our method. However, it is not hold true due to the following reasons.

- When cells are subdivided into infinitesimal ones, the boundaries of a cell approach straight coplanar lines [see Fig. 9(g), (j) and (m)]. Hence, the Euclidean geometry is possible to be used to measure infinitesimal cells. As illustrated in Fig. 4, vertices of infinitesimal cells could represent boundaries and could be used to measure the shape regularity of cells. Further numerical results (see Fig. 12 in Section 3.2) imply that the metric AveRaComp of cells is a monotonically increasing function. That means infinitesimal cells are more representative of shape regularity than large cells.
- For a given spherical tessellation, the boundaries of cells are of meaning [usually straight lines on projection plane(s), geodesics, or graticules] and definite. Hence, it is unreasonable to change the boundaries of cells while maintaining the points used in our metric. Modification boundaries of an existing tessellation may improve shape regularity of some cells [e.g., see Fig. 9(j)], but shape regularity of other cells [e.g., see Fig. 9(g)] would probably be damaged. Further calculation (see Appendix A) implies that modification the boundaries has bad effects on shape characteristics.
- We could construct a tessellation that keeps midpoints fixed for some low levels of tessellations. Appendix A gives an analysis, and implies that the positions of midpoints of boundaries would change when subdivision goes further. Hence, it is difficult to conceive a tessellation which modifies the boundaries of cells for hierarchical tessellations, while simultaneously keeps the position of points for each level of tessellations.
- Additionally, modification of boundaries may have effects on areal distributions. Taking two octahedron-based methods in Fig. 6 for examples, O-QTM/Quad exhibits a less degree of shape distortions than OEAP/Quad, but O-QTM/Quad loses uniformity in area when compared to OEAP/Quad.

For the above reasons and some analyses mentioned in Section 2.3, it is fairly sensible to some extent that our metric AveRaComp measures the shape regularity of spherical tessellations.

2.5. Adaptation for spheroids

The derivations of formulae in Section 2.2 assume the Earth to be a sphere, however, the Earth is not an ideal sphere. Spheroids provide better approximations than sphere for the Earth. Given $\mathcal{E}$,

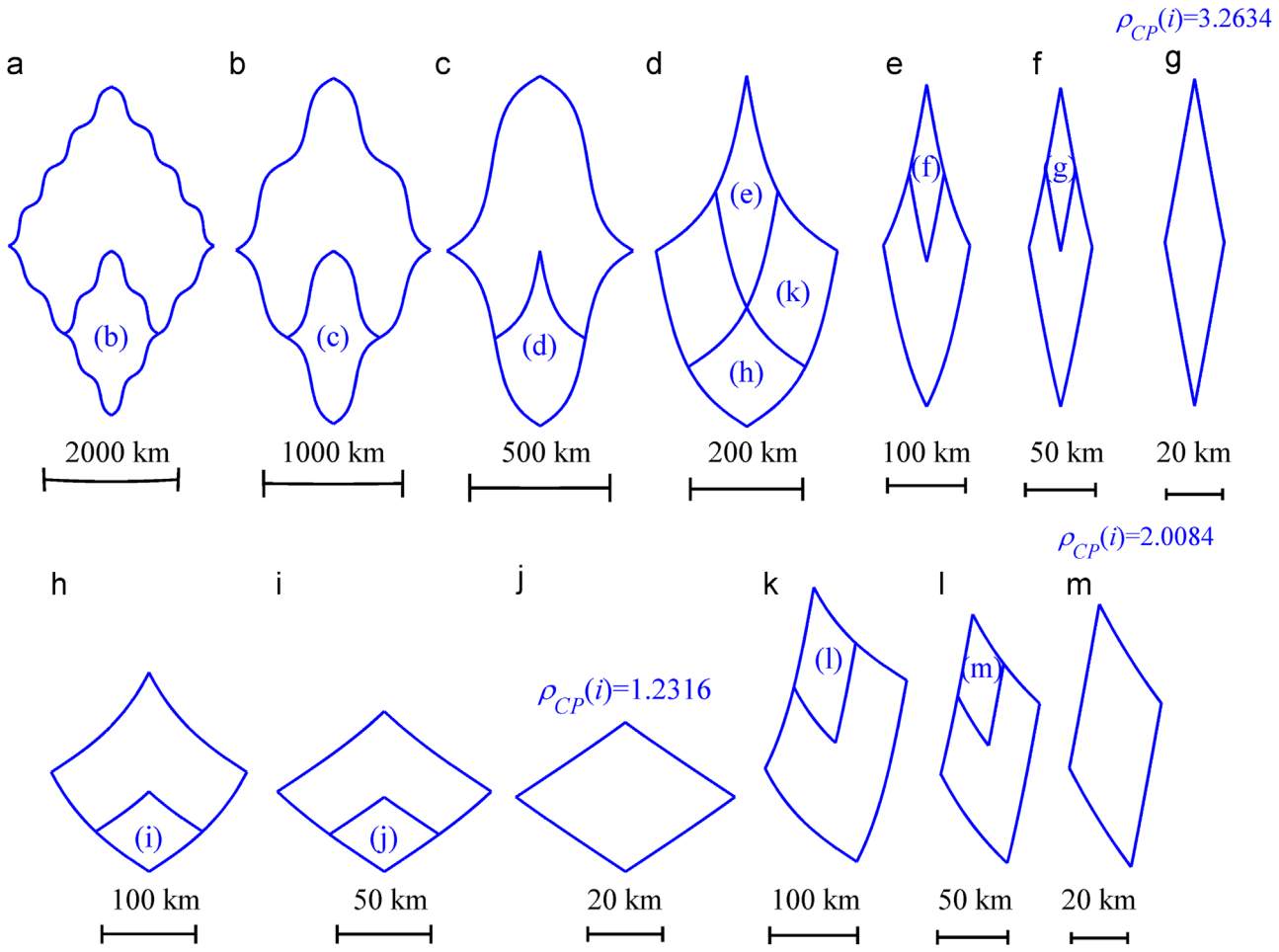

Fig. 9. Different level of subcells on a sphere. Even though a coarse cell exhibits some degrees of roughness on boundary, its subcells eliminate this factor by recursive subdivisions.

a reference ellipsoid, Snyder (1987) gives factors c_m and c_p to correct h and k (see Eqs. (8) and (9)), respectively.

$$c_m(\phi) = \frac{R}{a(1-e^2)}\sqrt{(1-e^2\sin^2\phi)^3}, \tag{15}$$

$$c_p(\phi) = \frac{R}{a}\sqrt{1-e^2\sin^2\phi}, \tag{16}$$

where R is the mean radius of $\mathcal{E}$, a is the radius along the semi-major axis of $\mathcal{E}$, e is the eccentricity of $\mathcal{E}$, and ϕ is latitude.

The calculations in Eqs. (1)–(5) depend on the assumption of the Earth being a sphere. When considering ellipsoid, small circle arcs in Eq. (5) turn to be elliptic arcs. The length of elliptic arcs could be calculated by using elliptic integral methods. But numerical integral is time consumed. So we simplify the process of calculating $\rho_{CP}(i)$ to adapt for ellipsoids (see Eqs. (17)–(19)). The simplification is numerical equivalent to Eqs. (1)–(5), while neither integral nor differential calculus) is introduced.

$$\rho_{CP}(i) \approx \tilde{\rho}_{CP}(i) = [\tilde{\rho}_{D3}(i) + \tilde{\rho}_{\alpha}(i)]/2, \tag{17}$$

$$\tilde{\rho}_{D3}(i) = \frac{\max\left(\left|\overrightarrow{P_1P_*}\right| + \left|\overrightarrow{P_*P_3}\right|, \left|\overrightarrow{P_2P_*}\right| + \left|\overrightarrow{P_*P_4}\right|\right)}{\min\left(\left|\overrightarrow{P_1P_*}\right| + \left|\overrightarrow{P_*P_3}\right|, \left|\overrightarrow{P_2P_*}\right| + \left|\overrightarrow{P_*P_4}\right|\right)}, \tag{18}$$

$$\tilde{\rho}_{\alpha}(i) = \cot\left(\frac{1}{2}\arccos\left|\frac{\overrightarrow{P_1P_3}}{\left|\overrightarrow{P_1P_3}\right|}\cdot\frac{\overrightarrow{P_2P_4}}{\left|\overrightarrow{P_2P_4}\right|}\right|\right), \tag{19}$$

where i is the index of a spherical cell $\diamond P_1P_2P_3P_4$, and $\overrightarrow{P_sP_t}$ is the vector connecting points P_s, and P_t.

According to the analyses in Section 2.4, arcs on sphere approach to straight lines when cells are subdivided into infinitesimal ones. As a result, it makes sense that using the lengths of straight lines (see Eq. (18)) and the directions of straight lines (see Eq. (19)) to calculate our AveRaComp metric.

According to the correlation coefficient between ρ_{CP} and $\tilde{\rho}_{CP}$ (see Table 1), we find the simplified version of our AveRaComp metric could represent the original AveRaComp well [PPMCC(ρ_{CP}, $\tilde{\rho}_{CP}$) > 0.99998].

3. Experimental results and analyses

3.1. Overview of different tessellation methods

Table 3 summarizes some qualitative comparisons of different spherical tessellation methods. Here, eleven typical methods and their own inherent characteristics are listed. Other methods (Majewski et al., 2002; Platings and Day,

Table 3
Qualitative comparisons of 11 typical spherical tessellation methods.

Method	Author(s) (Year)	Category	Initial polyhedron	Shape of cells	NCB[a]	BG[a]	AE[a]	SR[a]
NUG	Rosca (2010)	MP-based	Two-hemispheres	Quadrilateral	n	No	Yes	No
USG	Roşca and Plonka (2011)	MP-based	Cube	Quadrilateral	n	No	Yes	No
Unicube	Ho et al. (2011)	MP-based	Cube	Quadrilateral	n	Yes	No	No
C-Sph	Ronchi et al. (1996)	MP-based	Cube	Quadrilateral	n	Yes	No	No
Isocube	Wan et al. (2007)	MP-based	Six-faces	Quadrilateral	n	No	Yes	No
OEAP	Holhoş and Roşca (2014)	MP-based	Octahedron	Triangle[b]	n	No	Yes	No
O-QTM	Dutton (1996)	MP-based	Octahedron	Triangle[b]	n	No	No	No
SQT	Fekete and Treinish (1990)	DSS-based	Icosahedron	Triangle[b]	2^{kc}	Yes	No	Yes
HEALPix	Górski et al. (2005)	MP-based	Twelve-faces	Quadrilateral	n	No	Yes	No
CitcomS	Zhong et al. (2000)	DSS-based	Rhombic dodecahedron	Quadrilateral	2^{kc}	Yes	No	Yes
Crusta	Bernardin et al. (2011)	DSS-based	Rhombictriacontahedron	Quadrilateral	2^{kc}	Yes	No	Yes

[a] NCB represents the number of cells on the boundary of one initial cell, where n is any positive integer, and k is any non-negative integer, BG represents whether the boundaries are geodesic or not, AE represents whether areas are equal or not, and SR represents whether subdivisions are recursive or not.

[b] It is possible to combine two adjacent triangular cells (e.g., Fekete and Treinish, 1990; Dutton, 1996; Holhoş and Roşca, 2014) as a quadrilateral cell. These varieties are denoted as SQT/Quad, O-QTM/Quad, and OEAP/Quad. The approach used by Majewski et al. (2002) is similar to Fekete and Treinish (1990).

[c] These methods subdivide a cell into four sub-cells, so the total number of cells in these methods could only be $4^k \cdot N_0$, where N_0 is the number of initial cells, and k is the time of tessellations. These methods are regarded as aperture-4 (Sahr et al., 2003) [or 4-fold Kimerling et al., 1999] subdivisions.

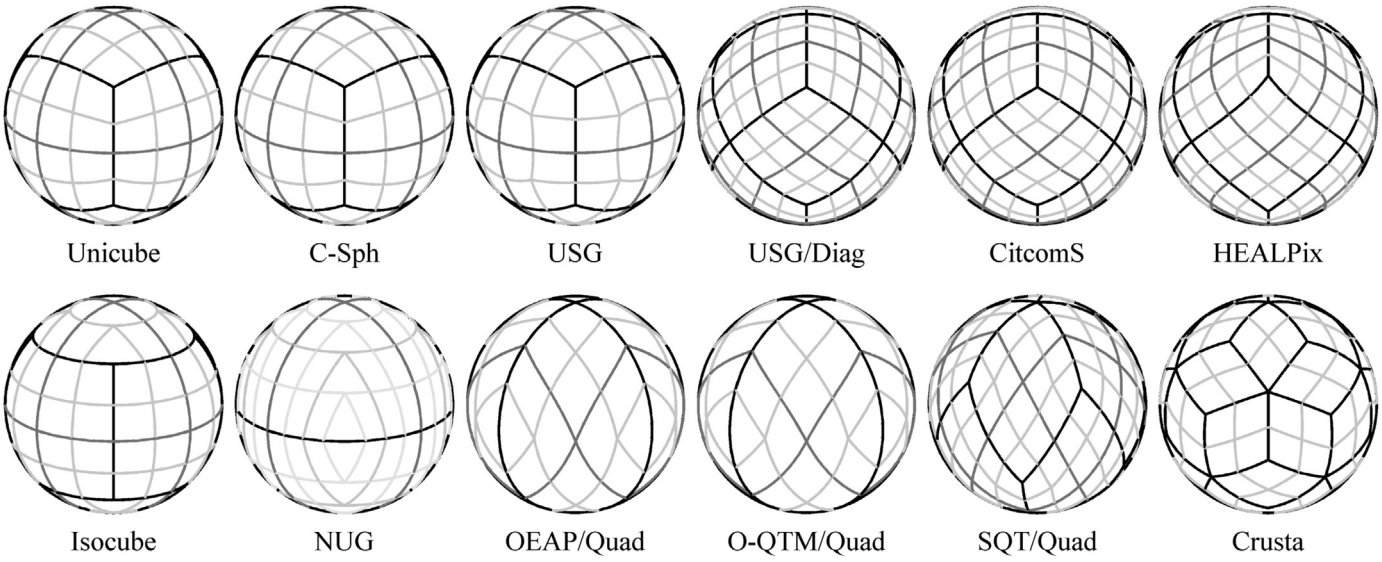

Fig. 10. Perspective views of different spherical tessellation methods [i.e., eight quadrilateral tessellations, three variants (named with a postfix "/Quad") of triangular tessellations, and a variant (named with a postfix "/Diag") of quadrilateral tessellations]. The variants of triangular tessellations are constructed by combining adjacent triangular cells. The variant USG/Diag is constructed by using diagonals of USG. Only aperture-4 subdivisions are illustrated. The dark black lines represent the first level of tessellations. The grids of Crusta are subdivided into the second level, and the grids of NUG are subdivided into the fourth level, while other grids are subdivided into the third levels of their own.

2004; Westerteiger et al., 2011) that are similar to some methods listed in Table 3 are not included. The methods in Table 3 involve commonly used polyhedrons, e.g., cube, octahedron, icosahedron, rhombic dodecahedron, and rhombic triacontahedron.

Fig. 10 depicts the perspective views of eight spherical quadrilateral tessellations listed in Table 3. In addition, USG/Diag (which is based on rhombic dodecahedron) and variants (i.e., SQT/Quad, O-QTM/Quad, and OEAP/Quad) of three triangular tessellations are also illustrated in Fig. 10.

3.2. Evaluation of shape regularity and distortions of texels

Fig. 11 illustrates the distributions of our metric AveRaComp for some more tessellation methods besides those methods depicted in Fig. 6. Due to symmetry, we only plot one initial cell [see Fig. 11 (d)] for each method. From Fig. 11(a)–(c), we note that our metric is discontinuous in some DSS-based methods. Further analysis implies that distributions of normalized areas for DSS-based methods are also discontinuous. Hence, DSS-based tessellations are not preferred choices to some extent.

When considering MaxAveRaComp according to Eq. (6), the evaluation results are illustrated in Fig. 12. For all methods we investigated, the number of cells to be evaluated is up to one billion cells (i.e., $4^{15} \approx 10.7 \times 10^8$) The horizontal axis of Fig. 12 represents the logarithm of the number of cells to the base of 4.

From Fig. 12, the metric MaxAveRaComp is a monotonically increasing function, so we could calculate the rankings of different spherical tessellation methods according to the supremum of the metric MaxAveRaComp (denoted by $\sup \rho_{CP}$).

The metric $\sup \rho_{CP}$ reflects the shape regularity of spherical tessellation methods. From Fig. 12, two DSS-based tessellations [i.e., rhombic dodecahedron based CitcomS (Zhong et al., 2000), and rhombic triacontahedron based Crusta (Bernardin et al., 2011)] surpass other methods we investigated according to $\sup \rho_{CP}$. In addition, cube-based USG (Roşca and Plonka, 2011), USG/Diag

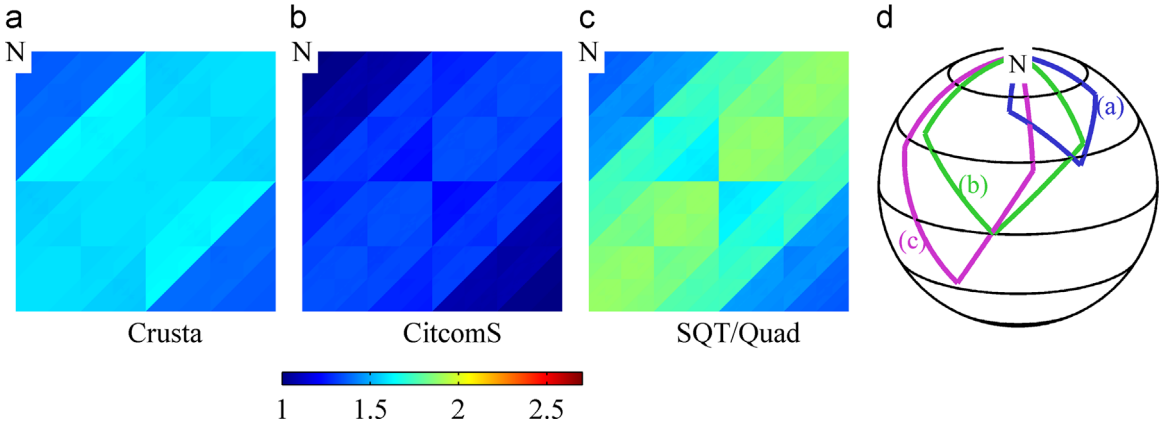

Fig. 11. Distributions of our AveRaComp metric as a supplementary illustration to Fig. 6 for more DSS-based tessellations. It should be noted that DSS-based tessellations exhibit some degrees of discontinuity in both shape regularity and area uniformity (from further calculations).

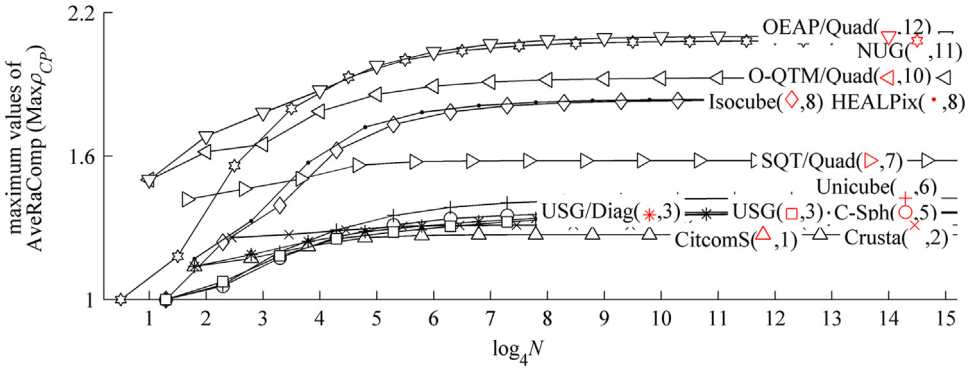

Fig. 12. Comparisons of shape regularity for different spherical tessellation methods up to one billion cells. The numbers in parentheses are the rankings of 11 different quadrilateral grids. The horizontal axis uses the logarithm of the number of cells to the base of 4 because aperture-4 subdivisions are investigated.

(which is based on rhombic dodecahedron), and cube-based C-Sph (Ronchi et al., 1996) are also good tessellations with quasi-regularity of shape.

Quadrilateral grids are suitable to construct quadtrees and map textures. This is commonly used in mapping a globe or environment mapping.

Generally, texels are squares in typical applications even when triangular cells are used because square texels are suitable for storage. In applications with textures, if a grid distorts to be rhombic, the texel distorts too. Therefore, the metric AveRaComp of quadrilateral grids (derived from triangular grids, or innate quadrilateral grids) may reflect the distortions of texture mapping.

To examine the distortions of texture mapping, we use NASA Blue Marble Next Generation (BMNG) dataset to map different spherical grids. Here, we examine two equal-area tessellation methods (USG and OEAP/Quad). The comparison of two equal-area methods eliminates the influences of non-uniformity of areas. The results of comparison are illustrated in Fig. 13.

In Fig. 13, BMNG dataset is firstly down-sampled to appropriate resolutions and then re-sampled according to specific projections [see Fig. 13(a) and (b)]. The times of texture re-sampling are approximately equal (i.e., $4 \times \delta_1^2 \approx 6 \times \delta_2^2$) for both USG and OEAP/Quad.

Next, the sampled textures are mapped on cells of the Earth. Local views of the Earth are demonstrated in Fig. 13(c)–(f).

From Fig. 13, OEAP/Quad exhibits more distortion and more aliasing than USG due to the shape irregularity of OEAP/Quad.

From above comparisons, we obtain that our shape metric measure the regularity of quadrilateral cells, and also reflect the associated distortions of texture mapping.

3.3. *Evaluating qualities of spherical cells considering both shape regularity and area uniformity*

The purposes of tessellations are both shape regularity and area uniformity. But it is impossible to achieve absolute perfection in both aspects (Kimerling et al., 1999; Platings and Day, 2004). A similar fact is that distortions are inevitable in any map projection (Snyder, 1987; Mulcahy and Clarke, 2001).

In addition to our shape metric, we also use χ_A, the coefficient of variation of spherical areas to evaluate the area uniformity of cells. Five equal-area tessellation methods [i.e., USG (Roşca and Plonka, 2011), HEALPix (Górski et al., 2005), Isocube (Wan et al., 2007), and OEAP (Holhoş and Roşca, 2014), and NUG (Rosca, 2010)] and the variants of these equal-area methods surpass other non-equal area methods we investigated. Following to those equal-area methods, Crusta (Bernardin et al., 2011; Ho et al., 2011), Unicube, and Unicube/Diag are quasi-equal-area methods.

Fig. 14 illustrates shape regularity and area uniformity of different tessellation methods on a two dimensional coordinate system. Here, we employ sup χ_A, the supremum of the coefficient of variation of spherical areas to evaluate area uniformity. From characteristics of rotation-invariant mentioned above, and further calculations of areas, variants of methods with a postfix "/Diag" that are listed in Table 2 have the same qualities (same positions in Fig. 14) as their original methods.

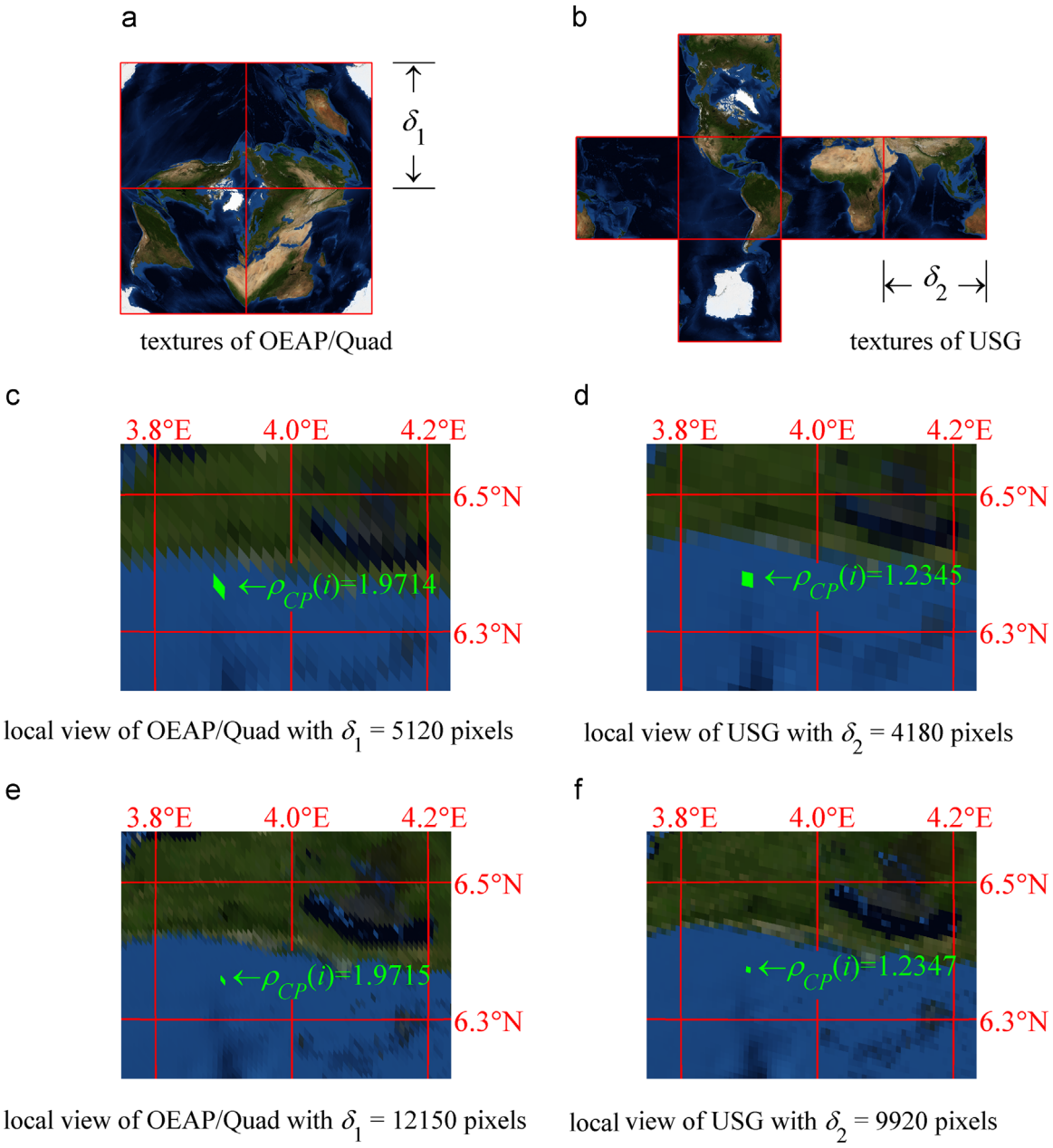

Fig. 13. Texture distortions of two equal-area tessellations (OEAP/Quad and USG). The first row illustrates the sampled textures of OEAP/Quad (resolution is $4 \times \delta_1^2$) and USG (resolution is $6 \times \delta_2^2$), respectively. The last two rows give local views (looking at coast of Nigeria in western Africa from 10 km height and using 120° as the vertical field of view) of the Earth. We sample textures with approximately equal resolution for both OEAP/Quad and USG, i.e., $\approx$ 105 million pixels for the second row, and $\approx$ 590 million pixels for the third row. For a visually detectable comparison of local views, the texture sampling in the second row is insufficient. There is a detectable aliasing along horizontal coastline in (c), while aliasing is not obvious in (d). Green arrows in the last two rows indicate four cells to be measured via the metric $\rho_{CP}(i)$. Although the metrics $\rho_{CP}(i)$ of these local views (i.e., about 1.97 for OEAP/Quad, and about 1.23 for USG) are less than the metrics $\sup \rho_{CP}$ (i.e., about 2.10 for OEAP/Quad, and about 1.36 for USG), OEAP/Quad exhibits more distortions and more aliasing than USG. (For interpretation of the references to color in this figure caption, the reader is referred to the web version of this paper.)

We also evaluate spherical tessellations on WGS84 reference ellipsoid by using our AveRaComp metric and area uniformity metric. The area of cells is corrected by multiplying area by the product of c_m and c_p (see Eqs. (15) and (16)). The AveRaComp of cells are calculated by using Eqs. (17)–(19).

From Fig. 14, we find that USG (Roşca and Plonka, 2011) and its variants ($\sup \rho_{D3} \approx 1.36$ and $\sup \chi_A = 0$) are good tessellations among methods we investigated when we consider both $\sup \chi_A$ and $\sup \rho_{CP}$.

Another three methods, i.e., Crusta (Bernardin et al., 2011), Unicube (Ho et al., 2011), and Unicube/Diag (that is not illustrated in Fig. 14), are also good choices [both (quasi) equal-area and quasi-regular tessellations] to some extent.

There is no significant difference between cells on sphere and cells on reference ellipsoid, compared to the difference among different tessellation methods. But a fact is that reference ellipsoid has relatively obvious influences for some methods (e.g., CitcomS).

4. Conclusions

The averaged ratio between complementary profiles (AveRaComp) is introduced to measure the distortion of map

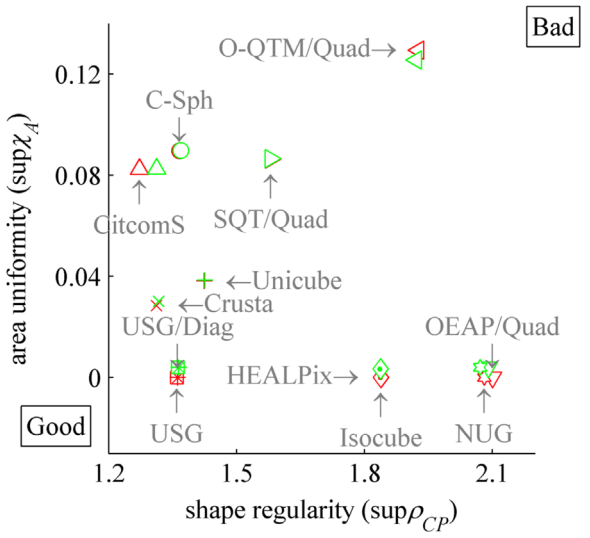

Fig. 14. Comparisons of shape regularity and area uniformity. We recommend USG for its advantages of quasi-regularity in shape and equal-area. Green markers indicate the results of evaluation when considering WGS84 reference ellipsoid. The difference between cells on sphere and cells on reference ellipsoid is minor, compared to the difference among different tessellation methods. (For interpretation of the references to color in this figure caption, the reader is referred to the web version of this paper.)

projections, and consequently, the shape regularity of spherical cells. Numerical analyses indicate that our metric AveRaComp results in high correlated distributions to differential calculus. It balances computational complexity and accuracy. Meanwhile, our metric avoids the mandatory restriction to map projection based tessellations when we employ Tissot indicatrix or differential calculus. Our shape metric is unified in form for map projection based or non-map-projection based tessellations (e.g., direct spherical subdivisions) and effective for evaluating different kinds of quadrilateral or triangular cells, although it is not suitable for hexagonal cells. A simplified version of AveRaComp metric is introduced to evaluate cells on ellipsoids. It provides a concise and general form to evaluate map projections and spherical tessellations. Our metric could also reflect the distortions of texels when we apply texture mappings to quadrilateral or triangular cells.

We quantitatively evaluate 11 typical spherical tessellation methods and some variants of these methods according to our shape metric and an essential area metric (χ_A, coefficient of variation of spherical areas). Further evaluation could also be applied to other existing or unborn methods.

Considering the maximum values of AveRaComp, rhombic dodecahedron based CitcomS, rhombic triacontahedron based Crusta, cubed-based Uniform Spherical Grids (USG) and Cubed Sphere, and rhombic dodecahedron based USG/Diag produce lower degrees of shape distortions than other methods we investigated.

Considering both shape regularity ($\sup \rho_{CP}$) and area uniformity ($\sup \chi_A$) on a two dimensional coordinate system, we recommend Uniform Spherical Grids and its variant for their optimal performances of areas uniformity and suboptimal performances of shape regularity. In addition, Crusta, Unicube map, and a variant of Unicube map are also preferred tessellation methods for their characteristics of (quasi) equal-area and quasi-regular.

Acknowledgments

We thank editors and reviewers for their kind help and critical review on our manuscript. This work is supported by the National Natural Science Foundation of China (NSFC) under Grant no. 61473013.

Appendix A. Modification of O-QTM/Quad

Firstly, we construct a 2D smooth and continuous transformation (see Eq. (A.1)) from (x, y) to (u, v) on a planar region, where $x \in [0.25, 0.5]$ and $y \in [0.25, 0.5]$.

$$\begin{cases} u = A \sin(4k\pi x - k\pi) + y \\ v = A \sin(4k\pi y - k\pi) + x \end{cases} \quad \text{(A.1)}$$

where $A > 0$ represents the amplitude of the sine function, and $k = 2^n$ represents the frequency, $n = 1, 2, \ldots$.

A planar tessellation using Eq. (A.1) is illustrated as Fig. A1 where parameter $A=0.005$, and $k=4$. Red cells represent primitive squares with equal areas on projection plane, blue cells are modified tessellation following Eq. (A.1). The cells are progressively refined from left to right, and could be subdivided further. In Fig. A1, black circles represent fixed corner points. It should be noted that the number of fixed points is finite.

If we want to increase the number of fixed points, we could increase the parameter k. The larger the parameter k, the more fixed points present. However, we notice that, in our example, when $N \geq 4 \times k^2$, the corners of blue cells deviate from the corners of red cells. When we choose a larger parameter k, another drawback is that boundaries exhibit a wavelike appearance when N is small. We could decrease amplitude parameter A, however, the wavelike appearance could not be fully eliminated since $A > 0$.

In addition to Eq. (A.1), we could construct other transformations that modify boundaries of cells. However, one could not make sure that all midpoints are fixed for all levels of tessellation. When N is large enough, the deviation of midpoints is inevitable.

The next step is constructing cells on the sphere. We could construct a variety of spherical cells by using different transformations. Here, we map the coordinate from (u, v) to (ϕ, λ) via inverse ZOT projection formulae (Dutton, 1991). Due to symmetry, we only consider cells on the north hemisphere.

Finally, we use our shape metric MaxAveRaComp to evaluate the shape regularity of modified cells illustrate in Fig. A1. The result of calculation is shown in Fig. A2. When $k=8$, our metric is larger than 3.5, the cell corresponding to the worst metric is illustrated as a blue cell in Fig. A2. The distortion of the blue cell is more severe than cells illustrated in Fig. 13.

From Fig. A2, we obtain that

(1) When $N \geq 16 \times k^2$ (see black circles), the metrics of modified cells are larger than the metric of primitive cells (the red line).

(2) There is a steep change when $k=8$. The larger the parameter k, the more steepness, and the larger the upper bound (over 3.5) of our metric.

The steepness and larger upper bound are caused by the wavelike feature of sine function mentioned above. If we would not like that to happen, we could decrease the amplitude parameter A. So, we keep the product of A and k, and reconstruct cells on the sphere. The results of keeping $A \cdot k = 0.01$ is that our metrics converge to a similar upper bound (about 1.78) for different A and k. However, a larger upper bound than primitive cells is inevitable (see red line in Fig. A2).

The above process is made to show that we could construct a tessellation with a finite number of fixed midpoints. However, when cells are subdivided further, the midpoints of cells must deviate from primitive cells. More seriously, cells could distort too much in the case of constructing a modified tessellation as mentioned above.

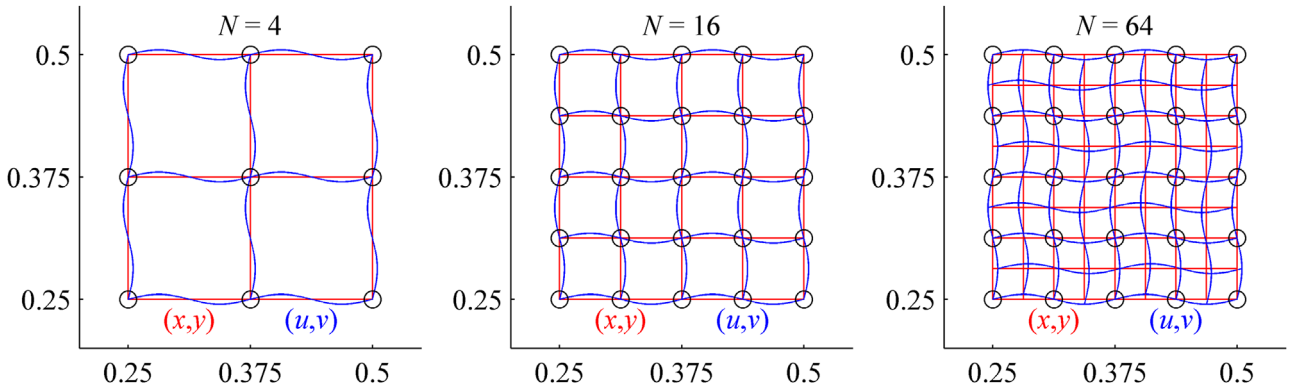

Fig. A1. Equally spaced cells on plane (in red), and modified cells with $A=0.005$, and $k=4$. Black circles indicate fixed corner points. When N exceeds a given value, the corners of blue cells are deviated from the corners of red cells. If we choose a larger parameter k, we obtain more fixed corner points. But boundaries exhibit a wavelike appearance when N is small. That is a drawback caused by keeping more points fixed. (For interpretation of the references to color in this figure caption, the reader is referred to the web version of this paper.)

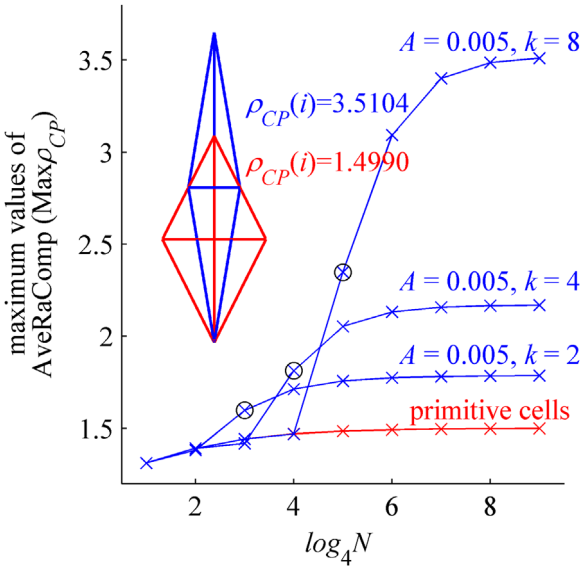

Fig. A2. The results of evaluating for spherical cells corresponding to planar cells shown in Fig. A1 via our metric MaxAveRaComp. The cell in blue is the worst cell when $A=0.005$, and $k=8$. This cell would exhibit more distortions than cells in Fig. 13(c). The cell in red is the primitive cell corresponding to the cell in blue. (For interpretation of the references to color in this figure caption, the reader is referred to the web version of this paper.)

References

Bahrainian, S.S., Dezfuli, A.D., 2014. A geometry-based adaptive unstructured grid generation algorithm for complex geological media. Comput. Geosci. 68, 31–37.

Bauer-Marschallinger, B., Sabel, D., Wagner, W., 2014. Optimisation of global grids for high-resolution remote sensing data. Comput. Geosci. 72, 84–93.

Bernardin, T., Cowgill, E., Kreylos, O., Bowles, C., Gold, P., Hamann, B., Kellogg, L., 2011. Crusta: a new virtual globe for real-time visualization of sub-meter digital topography at planetary scales. Comput. Geosci. 37 (1), 75–85.

Bösch, J., Goswami, P., Pajarola, R., 2009. RASTeR: simple and efficient terrain rendering on the GPU. In: Ebert, D., Krüger, J. (Eds.), Proceedings of Eurographics 2009. Eurographics Association, Munich, Germany, pp. 35–42.

Choblet, G., Čadek, O., Couturier, F., Dumoulin, C., 2007. ŒDIPUS: a new tool to study the dynamics of planetary interiors. Geophys. J. Int. 170 (1), 9–30.

Cignoni, P., Ganovelli, F., Gobbetti, E., Marton, F., Ponchio, F., Scopigno, R., 2003a. BDAM – batched dynamic adaptive meshes for high performance terrain visualization. Comput. Graph. Forum 22 (3), 505–514.

Cignoni, P., Ganovelli, F., Gobbetti, E., Marton, F., Ponchio, F., Scopigno, R., 2003b. Planet-sized batched dynamic adaptive meshes (P-BDAM). In: Turk, G., Van-Wijk, J., Moorhead, R. (Eds.), Proceedings of IEEE Conference on Visualization, IEEE, Seattle, Washington, pp. 147–154.

Clarke, K.C., 2000. Criteria and measures for the comparison of global geocoding systems. In: Goodchild, M.F., Kimerling, A.J. (Eds.), Proceedings of International Conference on Discrete Global Grids, Santa Barbara, California.

Dutton, G., 1991. Zenithial orthotriangular projection. In: Mark, D., White, D. (Eds.), Proceedings of 10th International Symposium on Computer-Assisted Cartography. ACSM & ASPRS, Bethesda, Maryland, pp. 77–95.

Dutton, G., 1996. Encoding and handling geospatial data with hierarchical triangular meshes. In: Kraak, M.J., Molenaar, M., Fendel, E.M. (Eds.), Proceedings of 7th International Symposium on Spatial Data Handling, Advances in GIS Research, vol. 2. Taylor & Francis, London, UK, pp. 505–518.

Fekete, G., Treinish, L., 1990. Sphere quadtrees: a new data structure to support the visualization of spherically distributed data. In: Farrell, E.J. (Ed.), Extracting Meaning from Complex Data: Processing, Display, Interaction vol. 1259. SPIE, Bellingham, Washington, pp. 242–253.

Gobbetti, E., Marton, F., Cignoni, P., Di Benedetto, M., Ganovelli, F., 2006. C-BDAM—compressed batched dynamic adaptive meshes for terrain rendering. Comput. Graph. Forum 25 (3), 333–342.

Goodchild, M.F., 1994. Geographical grid models for environmental monitoring and analysis across the globe (panel session). In: Proceedings of GIS/LIS. ACSM & ASPRS, Bethesda, Maryland.

Goodchild, M.F., Yang, S., 1992. A hierarchical spatial data structure for global geographic information systems. CVGIP: Graph. Models Image Process. 54 (1), 31–44.

Górski, K.M., Hivon, E., Banday, A.J., Wandelt, B.D., Hansen, F.K., Reinecke, M., Bartelmann, M., 2005. HEALPix: a framework for high-resolution discretization and fast analysis of data distributed on the sphere. Astrophys. J. 622 (2), 759–771.

Goswami, P., Makhinya, M., Bösch, J., Pajarola, R., 2010. Scalable parallel out-of-core terrain rendering. In: Ahrens, J., Debattista, K., Pajarola, R. (Eds.), Proceedings of Eurographics Symposium on Parallel Graphics and Visualization. Eurographics Association, Norrköping, Sweden, pp. 63–71.

Gregory, M.J., Kimerling, A.J., White, D., Sahr, K., 2008. A comparison of intercell metrics on discrete global grid systems. Comput. Environ. Urban Syst. 32 (3), 188–203.

Ho, T.-Y., Wan, L., Leung, C.-S., Lam, P.-M., Wong, T.-T., 2011. Unicube for dynamic environment mapping. IEEE Trans. Vis. Comput. Graph. 17 (1), 51–63.

Holhoş, A., Roşca, D., 2014. An octahedral equal area partition of the sphere and near optimal configurations of points. Comput. Math. Appl. 67 (5), 1092–1107.

Hwa, L.M., Duchaineau, M.A., Joy, K.I., 2005. Real-time optimal adaptation for planetary geometry and texture: 4–8 tile hierarchies. IEEE Trans. Vis. Comput. Graph. 11 (4), 355–368.

Kimerling, A.J., Sahr, K., White, D., Song, L., 1999. Comparing geometrical properties of global grids. Cartogr. Geogr. Inf. Sci. 26 (4), 271–288.

Majewski, D., Liermann, D., Prohl, P., Ritter, B., Buchhold, M., Hanisch, T., Paul, G., Wergen, W., Baumgardner, J., 2002. The operational global icosahedral-hexagonal gridpoint model GME: description and high-resolution tests. Mon. Weather Rev. 130 (2), 319–338.

Mulcahy, K.A., 2000. Two new metrics for evaluating pixel-based change in data sets of global extent due to projection transformation. Cartographica 37 (2), 1–11.

Mulcahy, K.A., Clarke, K.C., 2001. Symbolization of map projection distortion: a review. Cartogr. Geogr. Inf. Sci. 28 (3), 167–182.

Oldham, D., Davies, J.H., Phillips, T.N., 2012. Generic polyhedron grid generation for solving partial differential equations on spherical surfaces. Comput. Geosci. 39, 11–17.

Platings, M., Day, A.M., 2004. Compression of large-scale terrain data for real-time visualization using a tiled quad tree. Comput. Graph. Forum 23 (4), 741–759.

Ronchi, C., Iacono, R., Paolucci, P.S., 1996. The "cubed sphere": a new method for the solution of partial differential equations in spherical geometry. J. Comput. Phys. 124 (1), 93–114.

Rosca, D., 2010. New uniform grids on the sphere. Astron. Astrophys. 52 (A63), 1–4.

Roşca, D., Plonka, G., 2011. Uniform spherical grids via equal area projection from the cube to the sphere. J. Comput. Appl. Math. 236 (6), 1033–1041.

Sahr, K., White, D., Kimerling, A.J., 2003. Geodesic discrete global grid systems. Cartogr. Geogr. Inf. Sci. 30 (2), 121–134.

Snyder, J.P., 1987. Map projections: a working manual. Geological Survey Bulletin Series, U.S. Government Printing Office.
Teanby, N., 2006. An icosahedron-based method for even binning of globally distributed remote sensing data. Comput. Geosci. 32, 1442–1450.
Tegmark, M., 1996. An icosahedron-based method for pixelizing the celestial sphere. Astrophys. J. 470 (2), L81–L84.
Wan, L., Wong, T.-T., Leung, C.-S., 2007. Isocube: exploiting the cubemap hardware. IEEE Trans. Vis. Comput. Graph. 13 (4), 720–731.
Westerteiger, R., Gerndt, A., Hamann, B., 2011. Spherical terrain rendering using the hierarchical HEALPix grid. In: Garth, C., Middel, A., Hagen, H. (Eds.), Proceedings of IRTG 1131 Workshop – Visualization of Large and Unstructured Data Sets: Applications in Geospatial Planning, Modeling and Engineering, OpenAccess Series in Informatics, vol. 27. Schloss Dagstuhl–Leibniz–Zentrum fuer Informatik, Dagstuhl, Germany, pp. 13–23.
White, D., 2000. Global grids from recursive diamond subdivisions of the surface of an octahedron or icosahedron. Environ. Monit. Assess. 64 (1), 93–103.
White, D., 2006. Display of pixel loss and replication in reprojecting raster data from the Sinusoidal Projection. Geocarto Int. 21 (2), 19–22.
Zhong, S.J., Zuber, M.T., Moresi, L., Gurnis, M., 2000. Role of temperature-dependent viscosity and surface plates in spherical shell models of mantle convection. J. Geophys. Res. 105 (B5), 11063–11082.